

The Fabrication of Retina Phantoms for Sub- and Intra- Retinal Injections

Nancy T. Hoang* and Yuankai K. Tao

Department of Biomedical Engineering, Vanderbilt University, Nashville, TN

KEYWORDS. Retina, Phantoms, OCT, PDMS, AMD

BRIEFS. A retina phantom was made to mimic the mechanical and visual properties of a human retina under OCT to simulate retinal injection therapies.

ABSTRACT. Age-related macular degeneration (AMD) is the most prevalent retinal disease in people over the age of 50 in the developed world. AMD presents in two forms, neovascular and atrophic, causing impaired vision and blindness by damaging retinal microstructure. In neovascular AMD, blood vessel infiltration causes fluid leakage, scarring retinal tissues. In atrophic AMD, accumulation of lipofuscin deposits in the retinal pigmented epithelium (RPE) causes damage to the photoreceptors. While no treatment exists for either condition, recent studies suggest RPE stem cell injections in the retina can replace damaged cells making it a potential therapy for the late-stage of AMD. In this study, phantoms were created to simulate the layered structure of human retina. The phantoms were used as a testbed for studying and quantifying the utility of image-guided injection of therapeutics under optical coherence tomography (OCT) to simulate RPE stem cell surgery. These phantoms allowed for the quantification of injection fluid volume delivered during simulated sub- and intra- retinal injection as a method of integrating optical imaging data to guide drug delivery. This work can potentially benefit the accuracy and reproducibility of sub- and intra-retinal delivery of current-generation therapies. In addition, they allow for development in integration of OCT imaging and novel surgical maneuvers to provide real-time feedback that are correlated with postoperative functional outcomes.

INTRODUCTION.

Age-related macular degeneration (AMD) will affect an estimated 196 million people by 2020, making it one of the most prevalent retinal diseases in people over the age of 50 in the developed world [1-2]. AMD causes impaired vision and blindness by damaging retinal microstructure [3-4]. AMD presents in the neovascular “wet” form in 10% of cases and atrophic “dry” form in approximately 90% of cases [1, 5]. In neovascular AMD, abnormal blood vessels underneath the retina can grow and infiltrate past Bruch’s membrane (BM) [5], causing blood and fluid leakage in and between the retinal pigment epithelium (RPE) and lower layers of the retina [4-5]. This can eventually lead to choroidal neovascularization and, in late disease, new choroidal vessels can grow and penetrate the BM [6]. The vascular endothelial growth factor (VEGF), a protein causing the excess growth of blood vessels, has been identified as a cause for neovascular AMD. In the recent years, pegaptanib sodium, ranibizumab, and aflibercept have been used as anti-VEGF drug therapies, to inhibit the effects of the VEGF [7,-9]. In atrophic AMD, accumulation of drusen, yellow deposits consisting of lipofuscin, that build up over time in the RPE causes BM to distort and photoreceptors to break down [6,10]. Both conditions lead to geographic atrophy (GA), the late stage of AMD marked by large areas of RPE cell loss, and the progressive and permanent loss of photoreceptors and vision [6]. Although several treatments can slow the progression of neovascular AMD in the early stages, no current procedure exists to reverse the effects of GA in either conditions. RPE cells reside above BM, providing nutrients to and

maintaining the photoreceptors, thus, RPE cell death has been implicated in the progression from AMD to GA [12]. Pre-clinical trials in recent years have demonstrated the potential of using embryonic stem cell-derived RPE cells as a treatment for preventing vision loss [1, 11-12]. However, functional outcomes in animal models and clinical studies have been highly variable because difficulties in the delivery and diffusion of stem cells and genes to target areas limit therapeutic efficacy [12-13].

Optical coherence tomography (OCT) is currently the gold-standard for ophthalmic diagnostic imaging. OCT enables noninvasive high-resolution imaging of tissue microstructure with up to single-micron resolution without the use of exogenous contrast [14-16]. Over the last 25 years, the ophthalmology community has leveraged the high-speed and depth-sectioning capabilities of OCT to image weakly scattering tissues up to 1 mm beneath the surface of the retina in three-dimensions and volumetrically visualize deformations in tissue layers and progression of disease [17-19]. In addition to diagnostic imaging, OCT has also been used to track the *in vivo* efficacy of therapeutics and shown to be uniquely suited for guiding treatment in diabetic retinopathy, surgical planning, and predicting functional outcomes of pharmacologic and surgical treatment of ophthalmic diseases in the anterior segment and retina.

We hypothesize that OCT imaging would provide real-time feedback to guide sub- and intra-retinal injections and improve the efficacy and reproducibility of current-generation stem cell and gene therapies for GA. We developed a novel multi-layered retinal phantom to enable quantification of therapeutic volumes delivered in simulated surgical maneuvers as foundational studies for developing novel image-guided drug delivery methods and instrumentation.

Current materials used for the fabrication of tissue phantoms include hydrogels, such as gelatin and agarose, and 3-D printed silicones. Although hydrogels can be optically tuned, high refractive indexes poses as a barrier in the imaging process and material properties do not allow for the stiffness and elasticity needed for phantom functionality. In addition, rapid bacterial growth limits shelf-life of hydrogels [20]. Common 3-D printed silicones allow for adjusted material stiffness, however the process limits layer thicknesses needed to achieve micron thin layers [21-22]. Multi-layered phantoms were developed using PDMS (Polydimethylsiloxane), which has comparable refractive index to human tissue and can be tuned to simulate the mechanical properties of retinal tissue [23]. OCT-guided delivery of therapeutics during simulated sub- and intra-retinal injections in these phantoms allowed us to identify critical barriers to current-generation surgical techniques and provided a testbed for future technology development.

Three-dimensional OCT imaging data was analyzed in post-processing to precisely quantify injection volumes. Cross-sectional OCT images showing the injection site were segmented and visualized volumetrically to quantify the spatial extent of the delivered volume. OCT imaging dimensions were calibrated and used to calculate the total delivered volume, which was compared with the injected volume to model variability from compressible injection equipment (i.e., syringe and tubing) and, more significantly, fluid effusion from the injection

site. This data will enable development of predictive models for precise drug delivery to benefit personalized medicine and improve outcomes in ophthalmic surgery.

MATERIALS AND METHODS.

Optical scattering, stiffness, and layer thickness in the phantoms were adjusted by doping the PDMS with varying concentrations of TiO₂, varying PDMS cure-to-base ratios, and optimizing spin-coating parameters, respectively, to create phantoms that accurately replicated the layered structure of healthy human retina observed on OCT.

Optical Scattering.

PDMS (5 g base and 1 g cure) was titrated with 0.1-0.5 wt % of TiO₂ and manually mixed until homogenous. Each mixture was added to a 4 cm diameter petri dish and cured at 100° C for 4 hours. Samples were then imaged under OCT to quantify light scattering and matched to corresponding scattering layers within representative OCT cross-sections of normal human retina. An additional 0.8 grams of TiO₂ was added to the bottom layer (Layer 1) in order to compensate for loss of OCT contrast with increasing depth (Table SI).

PDMS Stiffness

Varying PDMS cure-to-base ratios were titrated in increments of 1 wt. %. Each mixture was added to a 4 cm diameter petri dish and cured at 100° C for 4 hours. Sample stiffness was then evaluated in compression, and 2 wt. % was identified as the cure-to-base ratio that mostly closely approximated human retinal stiffness.

Multi-layered PDMS Phantom

0.1 g of PDMS was placed on a glass coverslip and spin-coated before curing at 275°C for five minutes. PDMS cure was added immediately before spinning each layer to control for viscosity and spin-coat layer thickness. A 12 to 1 dilution of water to PVA-based glue (Elmer's, Westerville, OH) was added on top of each cured layer and spun at 4000 rpm for one minute. The cured slides were imaged with OCT and layer thickness were measured using a calibrated vertical translation stage with digital micrometer (Mitutoyo, Aurora, IL). The resulting data was fit to exponential models and used to extrapolate requisite spin speeds for target thicknesses.

Simulated Sub- and Intra- Retinal Injections

A custom micro-positioner was designed to provide precision 3-axis translation and 2-axis rotation control. Sub- and intra-retinal cannulas with 100/150 μm diameter (inner/outer) was attached to a syringe injection system (Harvard Apparatus, Holliston, MA) for controlled drug delivery at a rate of 8 mL/min. Cannula tips were localized under real-time OCT guidance with 2.7 μm axial resolution and 11 μm lateral resolution. The cannula was aligned to a static OCT imaging field-of-view and data was continuously acquired as the PDMS retinal phantom was translated into place for image-guided injection.

Injection Volume Quantification

OCT imaging dimensions were calibrated using a glass resolution test chart (USAF 1951, Edmund Optics, Barrington, NJ). The test chart was translated known displacements in three orthogonal axes using a kinematic stage and the corresponding pixel shift of features were measured on OCT. The intensity point-spread-function cross-section was used to identify the edge of the resolution bars and tracked in the x, y, and z-axes for pixel spacing calibration. OCT images of injection volumes were processed and segmented in post-processing using Avizo (Thermo Fisher Scientific, Waltham, MA) to quantify injection volumes.

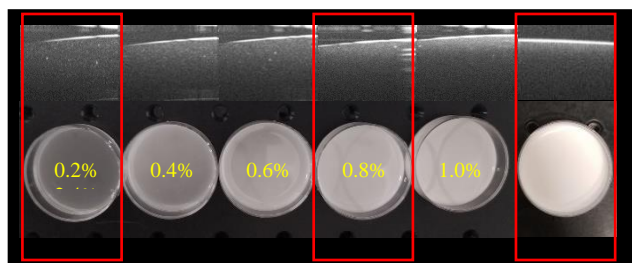


Figure 1. OCT images of scattering properties for different PDMS scattering levels. TiO₂ concentrations used to simulate low, medium, and high scattering retinal layers are outlined in red.

Table 1. Spin speeds and corresponding mean layer thicknesses in multi-layer phantoms (n=5).

Target Thickness (μm)	60	90	40	40	55	55	35
Measured Thickness (μm)	62	91	39	35.4	52	54.6	37.4
Spin Speed (rpm)	1850	1100	3100	2800	2350	1750	3600

RESULTS.

Low, medium, and high scattering levels were simulated using 0.2, 0.8, and 2.4 wt % of TiO₂ -to-PDMS base ratios, respectively (Fig. 1). A 2 wt % PDMS cure-to-base ratio was used to simulate retinal stiffness.

Multi-layered phantoms were fabricated using extrapolated spin speeds for target thicknesses identified using representative OCT cross-sections of normal human retina. Average phantom layer thicknesses variability was 4.8 μm (n=5) and likely resulted from surface tension differences between layers directly coating the cover glass and subsequent layers covering PDMS layers (Table 1).

Comparisons between OCT cross-sections of normal human retina and our multi-layer phantom show good correspondence in both layer thicknesses and scattering properties (Fig. 2). Higher scattering layers were used deeper in the phantom to compensate for depth-dependent differences in imaging contrast. Scattering intensities for both images were normalized and plotted.

Image-guided injections were performed in phantoms under OCT visualization. Retinal phantoms were submerged in water to minimize surface reflections and simulate vitrectomized eyes. OCT images of intra-retinal injection were segmented and volumetrically rendered for visualization (Fig. 3). Rendering shows lateral spreading of the injection volume, which was likely a result of phantom layer dissection by the injection pressure. Similar effects are observed surgically when creating a retinal bleb.

DISCUSSION.

In the study, TiO₂ was added to PDMS in order to create a phantom with similar optical properties as the human retina. TiO₂ concentrations ranged from 0.2-1.0 wt. %, and an additional 0.08 grams of TiO₂ was added to the bottom layer to compensate for depth-dependent differences in imaging contrast. Scattering properties between the human retina and phantom were compared to validate our model. Images were normalized by their respective noise floors to compensate for differ

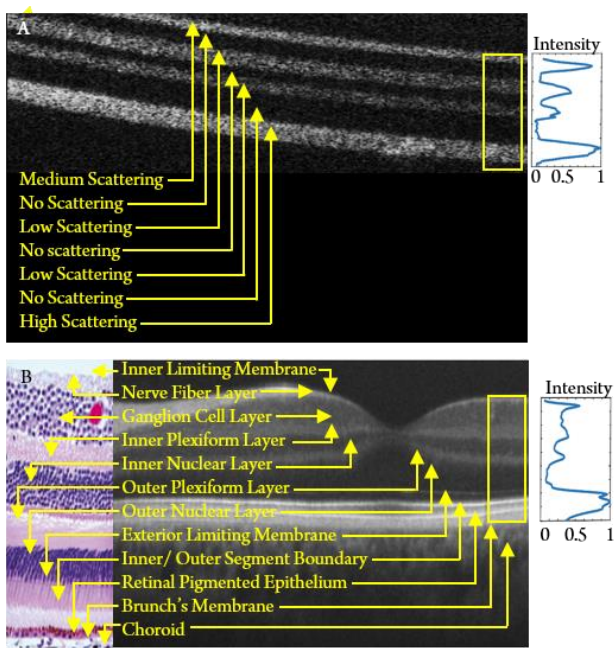


Figure 2. Comparison of OCT cross-sections of normal human retina and multi-layer retinal phantom. Horizontal average (yellow box) of normalized pixel intensity plot for visual comparison for (A) PDMS phantom and (B) corresponding human retinal OCT with representative histology showing layered microstructure in-depth.

ences in overall contrast. The human retina and phantom showed comparable OCT contrast for the respective layers (Fig. 2), but the phantom had higher scattering between layers. This was likely a result of the use of PVA-based glue between layers to ensure layer separation during injection simulations. Low PDMS cure concentrations were used to model retinal tissue stiffnesses but resulted in strong adhesion between phantom layers. The layer of PVA-based glue was used to reduce the amount of interlayer binding.

PDMS is known to have comparable mechanical properties as the human retina, making it the ideal substrate for a retinal phantom. However, the elastic modulus of PDMS is not consistent over a range of cure-to-base ratios. Lower concentrations of cure were used to reduce PDMS stiffness. In addition, TiO₂ displayed clumping and settling in final PDMS mixtures, which potentially affected scattering levels and layer thicknesses between phantoms. We compensated for these effects by mixing each mixture immediately before measuring scattering and spinning mixtures, but variabilities were still observed.

In our simulated injections, we performed two injections per phantom. The first to simulate a saline injection in the retinal phantom to separate the desired layers and create a retinal bleb. Then, a second injection was performed to simulate therapeutic agent delivered into the bleb, simulating current clinical standard-of-care sub- and intra-retinal injection techniques. In addition to the simulated injections performed in this study, our phantom may be directly applied to investigate novel methods for precise layer separation during bleb formation. Injection dynamics in retinal phantoms showed that layer separation required build-up of sufficient pressure. This is similar to what is observed clinically in the dissection of retinal layers during retinal bleb creation. Thus, separation of sub- and intra-retinal delivery of therapeutics is divided between two injection procedures, bleb and drug delivery, to allow for precision control of delivered drug volume. In our simulated injections, the primary and secondary injections had comparable volumes, which we suspect resulted because the initial retinal dissection

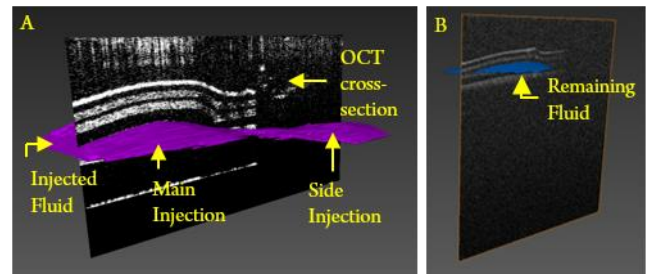


Figure 3. Volume rendering of the injection volume pre- and post-needle retraction (purple/ blue) with OCT cross-sections in two phantoms. (A) A total of $2.319 \times 10^{-4} \mu\text{L}$ was delivered between layers 1 and 2 before needle release. (B) A total of $5.369 \times 10^{-5} \mu\text{L}$ was delivered between Layers 3 and 4 before needle retraction.

limited the spatial extent of the second injection. Further work is needed prior to in vivo translation of these injection protocols.

CONCLUSION.

Retinal phantoms provide a testbed for future technology development and can be used to guide sub- and intra-retinal injections under OCT in real-time. This work presented methods for developing a multi-layered retinal phantom that simulates optical scattering, thickness, and material properties of the human retina. The utility of this phantom was then demonstrated in simulated image guided retinal injections using OCT. The phantom provided a stable and robust test-bed for real-time guidance of sub-retinal injections and quantification of key injection parameters. By studying simulated injections, the effectiveness and reproducibility of current-generation stem cell and gene therapies for GA can be improved. Moving forward, the methods and results in this work will be used to better understand dosing and administration of sub-retinal injections for animal and human studies and can be used to develop personalized drug delivery and therapeutics protocols for next-generation ophthalmic treatments.

ACKNOWLEDGMENTS.

I would like to thank Dr. Kenny Tao, Joe Malone, and the rest of the members of the DIGII Lab for giving me this opportunity and guiding me throughout my research. I would also like to thank Dr. Brown, Dr. Campbell, and the SSMV for supporting me through this journey.

SUPPORTING INFORMATION.

TiO₂ concentrations for corresponding retinal layers in PDMS phantoms.

REFERENCES

- [1] Brightfocus, Age-Related Macular Degeneration: Facts & Figures (2018). (Available at <https://www.brightfocus.org/macular/article/age-related-macular-facts-figures>).
- [2] National Eye Institute, Facts About Age-Related Macular Degeneration (2015). (Available at https://nei.nih.gov/health/maculardegen/armd_facts).
- [3] A.H. Koh and C.L. Ang, Age-related macular degeneration: What's new. (2002). (Available: <https://www.ncbi.nlm.nih.gov/pubmed/12061304>).
- [4] G. S. Hageman, Ed., *Webvision: The Organization of the Retina and Visual System [Internet]*. (University of Utah Health Sciences Center, 2008).
- [5] P. Storey, L. Hark, J. A. Haller, "[Age-related Macular Degeneration: An Overview]" in *Handbook of Nutrition, Diet and the Eye* (Academic Press, Cambridge, MA, ed. 1, 2014), pp 11-20.
- [6] P. Kaszubski, T. Ben Ami, C. Saade, R.T. Smith, Geographic atrophy and choroidal neovascularization in the same eye: a review. *Ophthalmic research*. **8**, 185-193 (2016).

- [7] CATT Research Group, Ranibizumab and bevacizumab for neovascular age-related macular degeneration. *The New England Journal of Medicine*. **20**, 1897-1908 (2011).
- [8] D. Shukla, P. Namperumalsamy, M. Goldbaum, and E.T. Cunningham, Pegaptanib sodium for ocular vascular disease. *Indian journal of ophthalmology*. **55**, 427-430 (2007).
- [9] M. McKibbin, H Devonport, R Gale, M Gavin, A Lotery, S. Mahmood, P. Patel, A. Ross, S. Sivaprasad, J. Talks, and G. Walters, Aflibercept in wet AMD beyond the first year of treatment: recommendations by an expert roundtable panel. *Eye*. **29** (2015).
- [10] *American Academy of Ophthalmology*, What Are Drusen? (2018). (Available at <https://www.aao.org/eye-health/diseases/what-are-drusen>).
- [11] P.D. Westenskow, T. Kurihara, and M. Friedlander, “[Utilizing stem cell-derived RPE cells as a therapeutic intervention for age-related macular degeneration]” in *Retinal Degenerative Diseases. Advances in Experimental Medicine and Biology* (Springer, New York, NY, vol. 801 2014), pp. 323-329.
- [12] R. E. MacLaren, J. Bennett, and S. D. Schwartz, Gene therapy and stem cell transplantation in retinal disease: the new frontier. *Ophthalmology*. **123**, S98-S109 (2016).
- [13] B. Roska and J.-A. Sahel, Restoring vision. *Nature News*. **557**, 359-367 (2018).
- [14] D. Huang, E. Swanson, C.P. Lin, J. Schuman, W. Stinson, W. Chang, M. Hee, T. Flotte, K. Gregory, C. Puliafito, and J. Fujimoto, Optical coherence tomography. *Nature*. **254**, 1178-1181 (1991).
- [15] J. Fujimoto, C. Pitris, S. Boppart, and M. Brezinski, Optical coherence tomography: an emerging technology for biomedical imaging and optical biopsy. *Neoplasia*. **2**, 9-25 (2000).
- [16] C. Jayadev, N. Jain, S. Sachdev, A. Mohan, and N. Yadav, Utility of noninvasive imaging modalities in a retina practice. *Indian journal of ophthalmology*, **64**, 940-943 (2018).
- [17] K. Lurie, G. Smith, S. Khan, J. Liao, A. Ellerbee, Three-dimensional, distendable bladder phantom for optical coherence tomography and white light cystoscopy. *Journal of biomedical optics*. **19**, (2014).
- [18] J. Schuman, Spectral domain optical coherence tomography for glaucoma. *Transactions of the American Ophthalmological Society*. **106**, 426-458 (2008).
- [19] M. Wojtkowski, High-speed optical coherence tomography: basics and applications. *Optical Society of America*. **49**, D30-D61 (2010).
- [20] F. Esmonde-White, K. Esmonde-White, M. Kole, S. Goldstein, B. Roessler, and M. Morris, Biomedical tissue phantoms with controlled geometric and optical properties for raman spectroscopy and tomography. *The Analyst*. **136**, 4437- 4446 (2011).
- [21] A. Cloonan, D. Shahmirzadi, R. Li, B. Doyle, E. Konofagou, and T. McGloughlin, 3D-printed tissue-mimicking phantoms for medical imaging and computational validation applications. *3d Printing and Additive Manufacturing*. **1**, 14-23 (2014).
- [22] B. Doyle, T. Corbett, A. Cloonan, M. O’Donnell, M. Walsh, D. Vorp, T. McGloughlin, Experimental modelling of aortic aneurysms: novel applications of silicone rubbers. *Medical engineering & physics*. **31**, 1002-1012 (2009).
- [23] R. Palchesko, L. Zhang, Y. Sun, and A. Feinberg, Development of polydimethylsiloxane substrates with tunable elastic modulus to study cell mechanobiology in muscle and nerve. *PLOS One*. **7**, e51499 (2012).



Nancy Hoang is a student at John Overton High School in Nashville, TN; she participated in the School for Science and Math at Vanderbilt University.